Simultaneous measurements of microwave photoresistance and cyclotron reflection in the multiphoton regime

Jie Zhang, Rui-Rui Du, L. N. Pfeiffer, and K. W. West

Phys. Rev. B **97**, 035437 — Published 25 January 2018

DOI: 10.1103/PhysRevB.97.035437

Simultaneous Measurements of Microwave Photoresistance and Cyclotron Reflection in the Multi-Photon Regime

Jie Zhang[1*], Rui-Rui Du[1,2], L. N. Pfeiffer[3], and K. W. West[3]

[1]*Department of Physics and Astronomy, Rice University, Houston, Texas 77251, USA*
[2]*International Center for Quantum Materials, Peking University, Beijing 100871, China*
[3]*Department of Electrical Engineering, Princeton University, Princeton,*
New Jersey 08544, USA

Abstract

We simultaneously measure photoresistance with electrical transport and coupled plasmon-cyclotron resonance (PCR) using microwave (MW) reflection spectroscopy in high mobility GaAs/AlGaAs quantum wells under a perpendicular magnetic field. Multi-photon transitions are revealed as sharp peaks in the resistance and the cyclotron reflection on samples with various carrier densities. Our main finding is that plasmon coupling is relevant in the cyclotron reflection spectrum but has not been observed in the electrical conductivity signal. We discuss possible mechanisms relevant to reflection or DC conductivity signal to explain this discrepancy. We further confirm a trend that more multi-photon features can be observed using higher carrier density samples.

PACS#
78.67.-n
79.20.Ws

* jz38@rice.edu

I. Introduction

Semiconductor interband/intraband transitions are traditionally studied via optical absorption and transmission. Nonlinear processes involving multiple photons attract tremendous attention not only for elucidating band structures beyond the experimentally attainable frequency range, but also for understanding the kinetic properties of solids in the presence of strong radiation.

With millimeter wave irradiation, non-equilibrium phenomena such as microwave-induced resistance oscillation (MIRO) [1,2] and zero-resistance states (ZRS) [3,4] were observed in two dimensional electron gases (2DEGs) over a decade ago. Theories have been advanced to explain their origin, the most popular being the displacement model proposed in [5] and the inelastic model in [6].

The demonstration of multi-photon cyclotron resonance (CR) corresponding to the rational values of $j = \omega/\omega_c = p/q = 1/2, 1/3, 2/3 \ldots$ (where ω is the MW frequency, ω_c is the cyclotron frequency, p and q are integers) via MW reflection spectroscopy [7] provides a unique method to probe this nonlinear process. Multi-photon CR is equivalent to sub-harmonic transitions in which the energy of q photons matches the spacing of p Landau levels (LLs) (see Fig. 1(b)). Experiments have been performed to study this phenomenon, but only using transport measurements. Dorozhkin et al. [7] proposed that sub-harmonic MIROs were suppressed below 30GHz due to single photon inelastic mechanisms when LLs start to overlap, yet the experiments of Zudov et al. [8] showed no frequency threshold. Wiedmann et al. observed high-order MIROs at temperatures up to 6.5K [9]. Although multi-photon processes usually happen at high intensities in the terahertz or infrared regime, they also occur due to large DC fields [10]. We generate this process in the absence of high AC or DC fields in a much lower frequency range where multi-photon transitions are prominent in high-mobility 2DEGs.

In the present work, a simultaneous measurement of PCR reflection and MIRO are undertaken on high mobility samples with different carrier densities. The prediction of multi-photon transitions facilitated by higher carrier density [11] is confirmed by both optical and electrical transport measurement. Power, frequency and temperature dependence are analyzed on a specific sample. The visibility of sharp signals from devices fabricated at varying widths enables us to tune the bulk plasmon frequency—a potential tool for coupling other fundamental excitations, for example, coupling composite fermions in the fractional quantum Hall states to photons in a detectable frequency range.

II. Experiments

The experiments are performed in GaAs/$\mathrm{Al_{1-x}Ga_xAs}$ quantum wells grown by molecular beam epitaxy. The specimens have carrier densities ranging from $0.8 \text{ to } 4 \times 10^{11}\ /\mathrm{cm}^2$ and mobility of about $10^7\ \mathrm{cm}^2/(\mathrm{V \cdot s})$ at 300 mK following 30 minutes of illumination under a red light emitting diode. The sample is inserted into a MW reflection interferometer (Fig. 1(a)). A similar schematic description of the MW interferometer can be found in [7] where the TE_{01} mode MW in the range of 26-40 GHz is transmitted and reflected through a WG28 waveguide. The incident MW field is divided by a magic tee which isolates the two collinear ports. The sample is mounted on a thin copper plate to increase reflectivity. An adjustable short is used to tune this interference sinusoidally at a fixed frequency. A sensor is mounted to the output port for power detection, the voltage of which is then fed into lock-in amplifier #2. We attach 8 indium contacts for standard transport measurement (lock-in amplifier #2) by annealing at 420 ℃ in forming gas. The amplitude modulation of the MW is provided by lock-in amplifier #1 at 100 Hz, which is much larger than 7 Hz used for lock-in amplifier #2 to measure photoresistance. A current of 1 μA is applied to the sample. The transport probe is top-loaded into a ^{3}He cryostat, which operates at a base temperature of 300 mK and is equipped with a 12 T superconducting magnetic coil. Thus we are able to perform simultaneous measurements of photoresistance and reflection at a given MW frequency by sweeping the external magnetic field.

The instrumental sensitivity was demonstrated in [11] revealing a visible transition under MW power as low as 10 nW on both 2DEGs and two dimensional hole gases (2DHGs). We again report successfully patterning mesoscopic structures by standard photolithography on samples without decreasing the signal/noise ratio. This is possible because the reflection setup obviates the need for sample thinning, which is required in conventional transmission spectroscopy.

III. Results and Discussion

A. General Considerations

Electrical transport and optical methods are common techniques to probe cyclotron transitions in a 2D system with LL spectrum of

$$E = \hbar\omega_c(N + \tfrac{1}{2}) \qquad (1).$$

When an integer multiple of MW frequency matches an integer multiple of the cyclotron frequency

$$\omega_c = eB/m^* \qquad (2),$$

where B the magnetic field and m^* is the effective mass of carriers, a resonance near the Fermi energy ε_F, occurs from the highest LL $|N_F\rangle \rightarrow |N_F + 1\rangle$ transition (Fig. 1(b)), resulting in a peak in both the optical and photoresistance spectra. By least-squares fitting the MIRO peaks to this linear dispersion, the effective mass of charge carriers can be extracted. It is well known that electrons in GaAs/AlGaAs quantum wells usually have an effective mass around 0.067 m_e, while hole effect mass varies between 0.2 m_e and 0.5 m_e, depending on materials parameters like well width and doping.

Due to the high mobility of samples, multi-photon transitions are clearly visible. A zero-resistance state is observed in Fig. 2(f), which is identified with sub-harmonic peaks corresponding to 2 and 3-photon absorption. The reflection signal in Fig. 1(c) also has multiple peaks related to fractional mode transitions. Transport parameters such as carrier density, mobility, and scattering time τ_{tr} are extracted from the magnetoresistance data in Fig. 1(d) while single particle relaxation time τ_s is obtained by fitting the cyclotron reflection trace with a Lorentzian. The ratio τ_{tr}/τ_s is greater than unity for each wafer, which indicates the dominance of small-angle scattering [15].

B. The Role of Metal Contacts

Multi-photon transitions are enhanced in strong electric fields and they can be observed under intense radiation or large DC electric fields. In our experiment, since indium contacts are used for transport measurements, the existence of a surface plasmon electric field near the metal contacts is possible when exposed to radiation.

When the large electric field of a surface plasmon at an interface interacts with photons, non-linear optical effects like second harmonics are observed [19]. In order to rule out the possibility that the multi-photon phenomenon is caused by the electric field of the surface plasmon near the contacts, which is relevant in many photovoltage measurements [20], we prepared different sample geometries for comparison. As shown in the bottom of Fig. 1(a), a large sample whose metal contacts are positioned outside of the region of MW radiation is used for comparison with a small sample cut from the same wafer whose contacts are under the radiation. No qualitative difference in terms of the sub-harmonic order in the MIRO transitions is found, except in small samples, additional peaks originating from the CR of electrons in the metal itself are observed. We further analyze the difference of cyclotron reflection signal with or without metal contacts, yet in both cases only slight modification of the peak strength is noted. Therefore, we conclude that metal contacts on a sample perimeter do not play an essential role in generating high harmonics or multi-photon processes in MIRO and cyclotron reflection measurements.

In fact, the electric field of surface plasmon on metallic thin films in the presence of MW is generally studied via transmission measurement on hole arrays, with or without enhancing mechanisms like grating. Since the size of the indium contacts in our experiment is less than 0.5 mm, which is much shorter than the wavelength of the MW, the electric field of surface plasmon is estimated to be on the order of $10^{-6}\ \mathrm{V/m}$ due to the lack of resonant mechanisms [16]. Note this is much weaker than the electric field provided by the DC bias.

Thus the phenomenon of multi-photon transitions in high mobility 2DEGs is a general result of interaction between 2D electrons from the highest LL and MW field.

C. Plasmon Coupling

Coupling between ω_c and the bulk magnetoplasmon frequency is widely observed in CR measurements. The bulk magnetoplasmon frequency is

$$\omega_p = \sqrt{\frac{n_s e^2}{2m^* \epsilon_{eff}} \frac{N}{W}}, \qquad (3)$$

where $N \in \mathbb{N}$ is the plasmon harmonic, n_s is the sheet carrier density, and $\epsilon_{eff} = (\epsilon_0 + \epsilon_1)/2$ is the effective dielectric constant, with the dielectric constant ϵ_1 of GaAs and ϵ_0 the dielectric constant of the vacuum) [12]. The effective resonance transition manifests itself as the coupled PCR mode

$$\omega = \sqrt{\omega_c{}^2 + \omega_p{}^2}. \qquad (4)$$

Parameters like effective mass and bulk magnetoplasmon frequency can be extracted by least squares fitting the resonant absorption peaks at different frequencies with this formula (Fig. 3). Note that the deduced effective masses in our samples are slightly larger than the well-known electron effective mass of 0.067 m_e (Table I). We think this discrepancy may be associated with the coupled PCR mode, therefore the deduced effective mass is not necessarily equal to the band mass. In addition, we observe the odd plasmon harmonic modes where $N = 1$, 3 and 5 in low density samples (Fig. 3(a)). However, the MIRO spectrum only shows the non-coupled cyclotron mode (Fig. 2). We note that there have been no theories proposed to explain the absence of coupled PCR modes in MIRO.

We interpret the difference in electric transport and cyclotron reflection measurements in essentially the same process as being due to different probing methods used. Therefore, even with the existence of all other physical processes, only the relevant part that could be coupled to the probing device would appear in certain measurements.

The difference between an optical reflection and electrical transport measurement under MW radiation is that the latter involves a DC electric field in addition to the rapidly oscillating AC field. Only those scattering processes that respond to the applied DC field would be relevant in the transport measurement. Note that though the MW has a large electric field (~10^4 V/m for

1mW power without accounting for the screening effect) compared to the DC field ($\sim 10^{-1}$ V/m for 1 μA current), the MW is oscillating with a very high frequency. Therefore the accumulation of Fermi sphere displacement caused by DC field in the Drude model (summed up in one cycle), dominates over the AC field, which could be regarded as unpolarized in its interactions with electrons. This phenomenon is the same with bulk magnetoplasmon, whose rapidly oscillating field does not polarize in a certain direction, whereas the DC electric field does. The lack of direct correlation between the magnetoplasmon and transport scattering processes may be a viable explanation for the absence of the coupled PCR mode in the MIRO spectra.

D. Multi-Photon Features in Higher Density Samples

From the linear dependence of the cyclotron frequency on the applied magnetic field in the MIRO measurements (Fig. 2), transition modes with different orders could be identified. Apart from the obvious fact that the number of visible high-order harmonic peaks depends on the mobility, or more precisely, the single particle quantum lifetime τ_s, the carrier density also plays an important role. In Fig. 2, we show that for wafers with carrier density lower than $1.3 \times 10^{11}\ \mathrm{cm}^{-2}$, no transition with j<1 is observed, whereas for densities greater than $2.7 \times 10^{11}\ \mathrm{cm}^{-2}$, two-photon transition (j=1/2) is always present, and even other fractional transitions like j=3/4 are observed in our highest density sample. Therefore, we conclude that higher carrier densities increase the observable orders of the multiphoton transitions in high mobility 2DEGs.

Surprisingly, our reflection interferometer reveals more orders of multi-photon cyclotron resonance signals than photoresistance. Limited by the fundamental mode frequency of the waveguide, the highest coupled PCR frequency we are able to observe is 40 GHz. So a smaller magnetoplasmon frequency would leave us a wider frequency range to work with. Compared to 2DHGs, the smaller effective mass in 2DEGs yields a higher plasmon frequency for millimeter size samples [11]. From equation (3), we can see that this value is determined by carrier density and the width of the sample for the same type of quantum well. Therefore, a lower density wafer (e.g. wafer a, b), is preferred when smaller size patterns are fabricated. In fact, for wafer b, resonance peaks are observed for the entire frequency range of 26-40 GHz on the 200 μm wide stripe sample, while when we push the plasmon frequency even higher by narrowing the width down to 100 μm, only 3 data points close to 40 GHz are collected (red dots in Fig. 3(c)). Therefore, a wafer which has lower density allows us to observe more coupled PCR modes. For high density samples (Fig. 3(c-f)), a single magnetoplasmon frequency with different cyclotron harmonics is identified, while for low density samples (Fig. 3(a)), odd plasmon harmonics (N=1, 3, 5) with a single cyclotron mode branch out in the dispersion. The different behavior of the coupling mode still requires theoretical explanation. However, j<1 transitions are found in high-density samples using a reflection signal, and much richer dispersion relations are apparent. Unlike transport data where the major peaks always correspond to the j=1 mode, coupled PCR data show a rather different response, where fractional j<1 transitions could well dominate over the fundamental j=1 cyclotron peaks.

Figure 4 shows a typical reflection signal at a fixed frequency and power on a sample cleaved from wafer e. Since the mobility is so high that peaks corresponding to different harmonic orders are well separated, Lorentzian shape fitting is possible for major features. Single particle relaxation time for each transition can be extracted from the full width at half maximum (FWHM) of each peak. The wide j=1/3 peak may associate to the process of subsequent absorption of two photons after the first one before the system relaxes to the ground state, therefore the effective broadening of the LLs ($\hbar/2\tau_s$) is almost 3 times that of j=1. The even smaller linewidth for j=3/4 or 4/5 is an interesting phenomenon which needs more theoretical investigations.

The fact that multi-photon processes and MIRO signal strength favor higher carrier density has been widely observed experimentally [8]. It can be simply understood as more electrons per unit area generate relatively higher signals. However, if we assume this nonlinearity comes from the electron-electron interaction, the ratio of Coulomb energy and kinetic energy is actually higher at low densities. Therefore, a proper theoretical framework is still needed to address the density dependence when multi-photon transitions are included in the picture.

E. Frequency, Power, and Temperature Dependences

On wafer c, where two-photon transitions are significant, we analyze MW power, frequency and temperature dependence of coupled PCR and MIRO signals. At a fixed frequency, both the signals increase with MW power (Fig. 5(a, b)), but in rather different manners. For MIRO, the major peak height (j=1) saturates at high MW power, which is consistent with the findings of Mani et al [13], while the j=1/2 peak is hardly visible with low radiation power. However in the case of MW reflection observed here, the dominant peak always corresponds to the two-photon process, which has no onset power threshold and in which the peak height depends linearly on the input power.

Figure 5(c) and (d) illustrate magnetoresistance and cyclotron reflection measurements at different frequencies with a fixed MW power. Two-photon MIRO peaks are more pronounced at lower frequencies. This is a reasonable result because the number of photons is inversely proportional to the frequency at the same power. However, this phenomenon is not observed in the reflection signal, where the major peak is always related to the two-photon transition in the frequency range. In spite of the fact that there is no frequency threshold for two-photon MIRO observed in our experiment, we cannot exclude the possibility that for separated LLs, there exists a higher frequency upper threshold of the form $\omega_c\left[1-\arccos(1-\alpha)-\sqrt{(2-\alpha)\alpha}\right],(\alpha<2)$ [9].

For a fixed MW frequency and power, increasing temperature will smear the MIRO peaks, but the reflection line shape remains the same within the experimental temperature range (Fig. 5(e, f)). SdHO, MIRO and cyclotron reflection are visible at different temperatures as their mechanisms are distinct. Within the investigated temperature, the CR reflection line shape remains unchanged as long as the temperature is low enough for electrons to undergo circular motion ($\omega_c\tau_q \gg 1$). SdHO can only be resolved at a lower temperature and a higher field when the LL separation ($\hbar\omega_c$) is larger than the smearing of the Fermi surface (k_BT). It has a form

$$\delta\rho = 4\rho_0 X_T \lambda \cos(2\pi\nu)/\sinh(X_T), \quad (5)$$

where $X_T = \frac{2\pi^2 k_B T}{\hbar\omega_c}$. In order to see MIRO, other than the conditions mentioned above, a strong MW radiation is required. The contribution to the photoresistance is

$$\delta\rho_i = -4\pi\rho_0 P_\omega^0 \frac{\tau_i}{\tau_{tr}} \epsilon_{ac} \lambda^2 \sin(2\pi\epsilon_{ac}) \qquad (6)$$

in the overlapping LL regime ($\omega_c\tau_q < \pi/2$), where $\tau_i = 3\tau_q^{im}$ in the displacement model and $\tau_i = \tau_{in}$ in the inelastic model [6]. Here τ_q^{im} is the long range impurity scattering time and τ_{in} is the electron-electron inelastic scattering time contribution to the single particle quantum lifetime τ_q.

F. Discussion of Simultaneous/Step-wise Transition in MIRO

When considering multi-photon processes, it is not known whether photons are absorbed simultaneously or stepwise. Dmitriev et al. [17] proposed that for well-separated LLs, sub-harmonic processes in MIRO are dominated by multi-photon inelastic mechanisms. However, MW-induced spectral reconstruction of density of states shows single photon transitions are possible when Landau levels start to overlap.

The underlying physics of these mechanisms are rather different. For a simultaneous absorption of m ($m \geq 2$) photons, the corresponding contribution to the photoresistance is ${W_\pm}^m$, where

$$W_\pm := \frac{\tau_q}{\tau_{tr}} \left[\frac{e\varepsilon v_F}{\hbar\omega(\omega_c \pm \omega)}\right]^2 \qquad (7)$$

(+ and – correspond to left and right circularly polarized radiation, respectively) [9]. While in the framework of stepwise transitions of m single photons, the ratio of inelastic photoresistance and DC resistance is

$$\frac{\delta\rho_{in}}{\rho_D} \propto \lambda^{2m} \qquad (8),$$

where $\lambda := \exp\left(-\frac{\pi}{\omega_c\tau_q}\right)$ is the Dingle factor [18].

Some parameters of the above-mentioned contribution could be estimated for wafer c. Transport scattering $\tau_{tr} \approx 1.3$ ns and quantum relaxation time $\tau_q \approx 0.7$ ps can be extracted from SdHO profiles. Note that the ratio τ_q/τ_{tr} is roughly 100 times smaller than the value presented in [9] due to the high mobility. The Fermi velocity is estimated at 2×10^5 m/s. Due to the screening effect, the magnitude of the electric field that the electrons experience is difficult to estimate directly. Damping of the SdHO could be used as a reference. Since we have a small quantum lifetime, the Dingle factor is vanishingly small ($\sim 10^{-31}$). Therefore, multi-photon inelastic mechanisms seem to be more probable for sub-harmonic processes in MIRO. In addition, the quasi-linear dependence of the two-photon peak height in MIRO at larger power for high frequencies indicates the significance of MW on the electron distribution function [6]. This is an important feature of the inelastic mechanism, further confirming our conjecture that sub-harmonic MIRO is dominated by the multi-photon inelastic processes. This is consistent with one-photon CR except it saturates at a lower MW power [6,9].

For wafer c, we also extract the single particle relaxation time $\tau_s \approx 0.3$ ns, responsible for LL broadening from Lorentzian fitting the cyclotron reflection line shape. It's the counterpart of, but much larger than, the quantum lifetime τ_q in MIRO. Within the experimental frequency range, the Dingle factor is approximately 0.96. Therefore, a model of stepwise absorptions of single photons before the electron system is completely relaxed seems more plausible--accounting for the two-photon peak in reflection spectra due to the long relaxation time in the strongly overlapped LL regime. The fact that two-photon peaks are higher than one-photon peaks also supports this long quantum relaxation time argument.

G. Multi-photon Cyclotron Transition Probability Calculation

With the constraint of energy conservation and high radiation intensity I, coherent multi-photon transitions between real initial and final states are allowed with the assistance of virtual intermediate states. Based on lowest-order perturbation theory, the n-photon absorption coefficient is $K^n \propto I^n$. When intensities become high, multi-photon absorption is comparable with single photon absorption. A nonlinearity parameter η_n could be introduced in this case,

$$\eta_n = \frac{K^n}{K^{n-1}} \qquad (9)$$

where K^n and K^{n-1} are photon absorption coefficients and the total absorption coefficient is

$$K = \sum_n K^n \qquad (10).$$

Unlike the lowest-order perturbation theory where K^n is determined by the absorption of n photons, to fully develop high-order nonlinearity, virtual transitions involve absorption of (n+m) photons and the simultaneous emission of m photons should also be considered. These absorption and emission channels interfere with and suppress each other, contributing to K^n substantially making the transition probability more complicated [14]:

$$W^n = \frac{nK^n I}{\hbar\omega} = \frac{m_*^{\frac{3}{2}}}{\pi\hbar^4} f(n\epsilon_0)(2n\hbar\omega)^{1/2}(M^n)^2. \qquad (11)$$

The high-order processes are contained in the matrix element

$$M^n \approx \frac{1}{4}\sqrt{\frac{2}{5}}\left(\frac{eE}{\omega}\right)^2 \frac{n+1}{n-1} \sum_{m=-\propto}^{+\propto} J_m(\rho_2^n) J_{n-2-2m}(\rho_1^n) \qquad (12)$$

with

$$\rho_1^n = \left(\frac{8n}{3m_*\hbar\omega}\right)^{1/2} \frac{eE}{\omega},\ \rho_2^n = \left(\frac{eE}{\omega}\right)^2 \frac{1}{2m_*\hbar\omega} \frac{n^2}{n^2-1}. \qquad (13)$$

Here $f(\epsilon)$ is the distribution function and $J_m(\rho)$ is the m-th order Bessel function, m_* is the effective mass and E is the electric field. This is under the assumption that $|M^n| \ll \hbar/\tau$. τ is the lifetime of the final state. In order to achieve - $\eta_n \approx 1$, intensity on the order of tens of GW/cm^2 is required, which lies far beyond the destructive threshold. However, in a lower frequency regime, much lower power intensity allows this transition. We believe it is the combination of our low frequency range and high sample mobility that makes the multi-photon processes visible in our experiments.

Increasing radiation intensity is obviously not preferred since heating might alter the dielectric properties of the sample. CR in high mobility GaAs quantum wells is a powerful approach to study multi-photon transitions, because the effective mass of the carriers has a stable value and the peaks are narrow.

IV. Conclusions

From a simultaneous measurement of photoresistance and optical reflection in a gigahertz regime, we observe multi-photon processes in high mobility 2DEGs where sub-harmonic transitions are identified by their magnetic field dispersion. We found that plasmon coupling is relevant in cyclotron reflection but not in MIRO spectra. Additionally, more orders of multi-photon transitions are revealed in higher carrier density samples, a result confirmed by both transport and optical experiments. Possible explanations are discussed. For a specific type of wafer, we show results of frequency, power and temperature dependencies. We further discuss theories put forward in explanation of the multi-photon transition mechanisms in the gigahertz frequency range.

Acknowledgements The work at Rice is supported by NSF Grant (No. DMR-1508644) and Welch Foundation Grant (No. C-1682). The work at Princeton is partially funded by the Gordon and Betty Moore Foundation as well as the National Science Foundation MRSEC Program through the Princeton Center for Complex Materials (No. DMR-0819860).

References

[1] M. A. Zudov, R. R. Du, J. A. Simmons, and J. L. Reno, Phys. Rev. B 64, 201311(R) (2001).

[2] P. D. Ye, L. W. Engel, D. C. Tsui, J. A. Simmons, J. R. Wendt, G. A. Vawter and J. L. Reno, Appl. Phys. Lett. 79, 2193 (2001).

[3] Ramesh G. Mani, Jürgen H. Smet, Klaus von Klitzing , Venkatesh Narayanamurti, William B. Johnson and Vladimir Umansky, Nature 420, 646-650, (2002).

[4] M. A. Zudov, R. R. Du, L. N. Pfeiffer and K. W. West, Phys. Rev. Lett. 90, 046807 (2003).

[5] Adam C. Durst, Subir Sachdev, N. Read and S. M. Girvin, Phys. Rev. Lett. 91, 086803 (2003).

[6] I. A. Dmitriev, M. G. Vavilov, I. L. Aleiner, A. D. Mirlin and D. G. Polyakov, Phys. Rev. B 71, 115316 (2005).

[7] S. I. Dorozhkin, J. H. Smet, V. Umansky and K. von Klitzing, Phys. Rev. B 71, 201306(R) (2005).

[8] M. A. Zudov, R. R. Du, L. N. Pfeiffer and K. W. West, Phys. Rev. B 73, 041303(R) (2006).

[9] S. Wiedmann, G. M. Gusev, O. E. Raichev, A. K. Bakarov and J. C. Portal, Phys. Rev. B 80, 035317 (2009).

[10] M.Khodas, H. -S. Chiang, A. T. Hatke, M.A. Zudov, M.G. Vavilov, L.N. Pfeiffer and K.W. West, Phys. Rev. Letts. 104.206801 (2010).

[11] J. Zhang, R. Liu, R.R. Du, L. N. Pfeiffer and K. W. West, Appl. Phys. Lett. 110, 142107 (2017).

[12] I. A. Dmitriev, A. D. Mirlin and D. G. Polyakov, Phys. Rev. B 75, 245320 (2007).

[13] R. G. Mani, C. Gerl, S. Schmult, W. Wegscheider and V. Umansky, Phys. Rev. B 81, 125320 (2010).

[14] ≪Intense Terahertz Excitation in Semiconductors≫ (Chapter 3) S. D. Ganichev and W. Prettl, Oxford University Press, 2006.

[15] S.D. Sarma and Frank Stern, Phys. Rev. B 32, 8442 (1985).

[16]] Bo Hou, Zhi Hong Hang, Weijia Wen, C. T. Chan and Ping Sheng, Appl. Phys. Lett. 89, 131917 (2006).

[17] I.A. Dmitriev, A.D. Mirlin and D.G. Polyakov, Phys. Rev. Letts. 99, 206805 (2007).

[18] I. V. Pechenezhskii, S. I. Dorozhkin and I. A. Dmitriev, JETP Lett. 85, 86-91 (2007).

[19] V. K. Valev, Langmuir. 28 (44), 15454–15471 (2012).

[20] Jian Mi, Jianli Wang, L. N. Pfeiffer, K. W. West, K. W. Baldwin and Chi Zhang, Phys. Rev. B 94, 125411 (2016).

Tables

Wafer	Carrier density ($10^{11}/\mathrm{cm}^2$)	Mobility ($10^6\mathrm{cm}^2/\mathrm{V}\cdot\mathrm{s.}$)	(m^*)	τ_{tr}(ps)	τ_s(ps)	τ_{tr}/τ_s
a	0.8	14	0.069	560	162	3.5
b	1.3	13	0.075	520	115	4.5
c	2.7	33	0.070	1310	300	4.4
d	3.6	4.7	0.069	187	53.6	3.5
e	4.1	11	0.072	450	114	3.9

Table I Description of electron samples **a**, **b c, d, e**. τ_{tr} and τ_s refer to transport scattering time and single particle relaxation time.

Harmonic order j	Peak width ΔB(T)	τ_s(ps)
1/3	0.0184	22.3
3/4	0.0036	113.8
4/5	0.0040	102.4
1	0.0059	69.4

Table II Fitting parameters of reflection peaks on sample cleaved from wafer e.

Figure captions:

FIG. 1. (a) Experimental schematic of simultaneous measurement of photoresistance and cyclotron resonance via a reflection interferometer. Below the configuration are a set of different geometries, of relative positions between the sample (green) and waveguide (black), including unpatterned sample with contacts beyond the waveguide (1), unpatterned sample with contacts

within the waveguide (2), unpatterned sample with no contact (3) and patterned sample with no contact (4). (b) Illustration of different transition orders. (c) Cyclotron reflection signal on a sample cleaved from wafer b, with a width of 1.7 mm at 32.2 GHz and 5 dbm, revealing multiple sub-harmonic transitions. (d) Transport data showing integer quantum Hall effect (IQHE) and fractional quantum Hall effect (FQHE) on sample a, b, c, d and e, from which the carrier densities and mobilities could be extracted. Symbol x denotes electron density in the unit of $10^{11}/\mathrm{cm}^2$.

FIG. 2. (a, b, c, d, e) MIRO peak fittings showing linear dependence of cyclotron frequency with respect to the magnetic field on samples cleaved from wafer a, b, c, d and e. (f) MIRO signal on a sample cleaved from wafer c, when irradiated with a fixed MW frequency of 40 GHz and a power of 5 dbm. High-order harmonics and sub-harmonic orders are labeled. Symbol x denotes electron density in the unit of $10^{11}/\mathrm{cm}^2$.

FIG. 3. Frequency dependence of the reflection peaks on the magnetic field on (a) a sample with width of 0.76 mm (unpatterned) cleaved from wafer a; (b) a sample cleaved from wafer a patterned with 200 μm wide stripes; (c) samples cleaved from wafer b patterned with 100 μm wide stripes (red line) and 200 μm wide stripes (other colors); (d) a sample with width of 1.7 mm (unpatterned) cleaved from wafer b; (e) a sample with width of 4.5 mm (unpatterned) cleaved from wafer c; (f) a sample with width of 2.1 mm (unpatterned) cleaved from wafer e. Insets are reflection signal line shapes at a fixed frequency (denoted in each figure) and constant MW power of 5 dbm.

Fig. 4. A typical reflection signal trace (red curve) with a fixed frequency of 35.8 GHz and power of 5 dbm on a sample cleaved from wafer e. Peaks are labeled by their transition orders, and fitted by Lorentzians. Fitting parameters are listed in Table II.

FIG. 5. Transport (upper panels) and reflection (lower panels) data on a sample cleaved from wafer c. (a, b) Power dependence with a fixed frequency of 33.5 GHz. (c, d) MIRO and reflection traces with selected frequencies. (e, f) Temperature dependence with a fixed frequency of 36 GHz and power of 5 dbm.

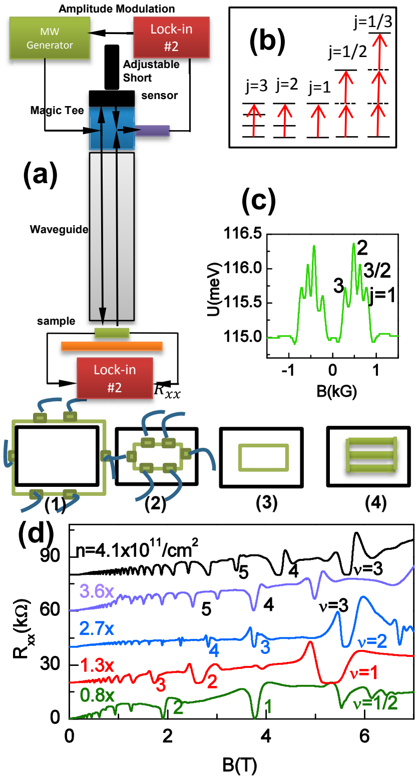
Amplitude Modulation
MW Generator
Lock-in #2
Adjustable Short
sensor
Magic Tee
(a)
Waveguide
sample
Lock-in #2
R_{xx}
(b)
j=1/3
j=1/2
j=3
j=2
j=1
(c)
116.5
116.0
115.5
115.0
U(meV)
2
3/2
3
j=1
-1
0
1
B(kG)
(1)
(2)
(3)
(4)
(d)
n=4.1x10^{11}/cm^2
90
60
30
0
R_{xx}(kΩ)
3.6x
2.7x
1.3x
0.8x
5
4
ν=3
5
4
ν=3
4
3
ν=2
3
2
ν=1
2
1
ν=1/2
0
2
4
6
B(T)

Figure 1

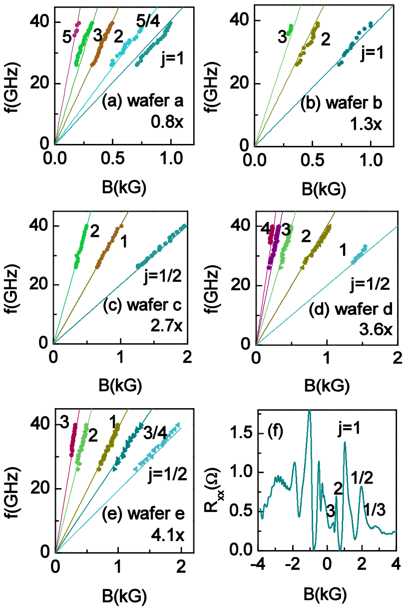

Figure 2   BJ13462   16JAN2018

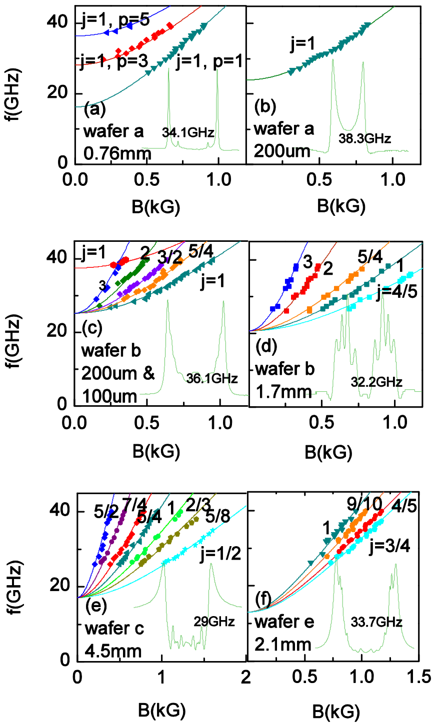

Figure 3 BJ13462 16JAN2018

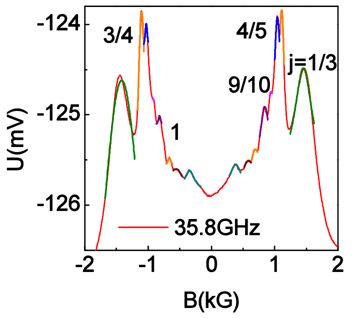

Figure 4 BJ13462 16JAN2018

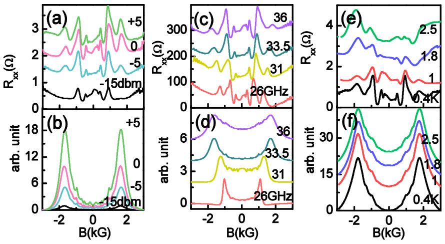

Figure 5 BJ13462 16JAN2018